ACS APPLIED MATERIALS & INTERFACES

www.acsami.org Research Article

Interface Reaction in Core−Shell Boron−FeF_3: Direct Observation of Gas Release and Oxide Removal during Combustion

Lei Yang,[#] Yuan Qin,[#] Gabriel Lopez, Erik Hagen, and Michael R. Zachariah*

Cite This: https://doi.org/10.1021/acsami.5c18742 Read Online

ACCESS | Metrics & More | Article Recommendations | SI Supporting Information

ABSTRACT: Boron is a high-energy fuel, but its persistent B_2O_3 surface oxide shell suppresses ignition and combustion. Here, we present a promising strategy for improving the performance of boron-based nanoenergetics. $FeF_3 \cdot xH_2O$-coated boron nanoparticles ($B@FeF_3 \cdot xH_2O$) are synthesized with a one-pot method and incorporated into 3D-printed thermite composites. Thermogravimetric analysis and T-jump ignition testing show that the $FeF_3 \cdot xH_2O$ coating reduces the onset temperature of boron oxidation by >70 °C, while the combustion regression rates of 3D-printed thermites increased by up to 55%. High-speed digital inline holography and color pyrometry capture the in-flight particle fragments leaving the flame front and observe violent droplet explosions due to rapid gas release. T-jump time-of-flight mass spectrometry confirms HF and BF_2 evolution, indicating BF_3 gas generation and B_2O_3 removal. These findings reveal that fluorinated coating enhances boron combustion via oxide etching and gas expansion, providing both mechanistic and strategic insights for boron-based nanomaterials.

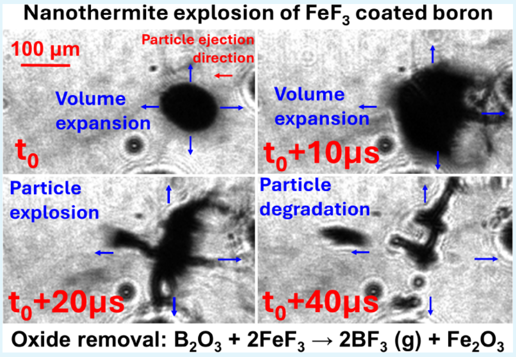

KEYWORDS: *boron, surface modification, holography, energetic materials, combustion*

1. INTRODUCTION

Nanoscale metals and metalloids, such as Al, Ti, Mg, B, and Si, have been extensively investigated as high-energy fuels in nanoenergetic composites for propellant and pyrotechnic applications.[1−5] Among these, boron is considered a particularly attractive candidate for propellant and explosive additives due to its exceptionally high gravimetric and volumetric enthalpies of oxidation (59 $kJ \cdot g^{-1}$ and 138 $kJ \cdot cm^{-3}$).[4,6] Despite its thermodynamic advantages, boron suffers from poor ignition and combustion behavior, which is primarily attributed to the presence of a native oxide shell (B_2O_3) that forms a nonvolatile layer upon heating.[4,7] With a relatively low melting point (∼450 °C) and high boiling point (∼1860 °C), this liquid B_2O_3 persists during combustion, acting as a diffusion barrier that isolates the reactive boron core from incoming oxidizers,[4,7] which leads to constrained energy release during combustion.

Reducing the particle size of metal fuels is a widely adopted strategy to enhance ignition sensitivity and combustion performance due to increased surface area and shorter diffusion paths.[1,3,4] However, size reduction also leads to higher oxide content and increases agglomeration during combustion,[3,8] which necessitates tailored surface modification strategies.[9−16] Previous research studies have explored a variety of fluorine-bearing additives and coatings that have been shown to improve reactivity by disrupting the B_2O_3 shell.[14−22] For example, fluoropolymers and fluoride salts (including transition metal fluorides such as NiF_2, CoF_2, and BiF_3) have demonstrated promising results in enhancing ignition and combustion efficiency.[5,13−17] The size-dependent behavior parallels our earlier findings on aluminum, where we extended studies from micron-sized Al to nanoparticles and demonstrated that applying transition metal coatings (e.g., Ni, Co, Cu) could trigger intermetallic reactions, reduce ignition thresholds, and promote alumina shell disruption.[11,12] Analogously, we propose that coating nano-B with transition metal fluorides could enable similar enhancements by chemically activating the surface and improving reaction propagation. Among these candidates, FeF_3 is found to be quite effective according to the thermal analysis by Qin et al.,[17] which shows that the oxidation reaction temperature of micron-B gets a reduction up to 191 °C with FeF_3 coating. The proposed mechanism involves the etching reaction of FeF_3 with B_2O_3, while concurrently producing Fe_2O_3, a known burn rate catalyst.[17] It should be noted that these strategies may not directly translate to nanoboron, which remains less explored.[13−17] More importantly, although surface-modification of micron-B has been widely explored with various fluorinated species,[14−21] current studies still lack direct experimental

Received: September 18, 2025
Revised: November 18, 2025
Accepted: December 16, 2025

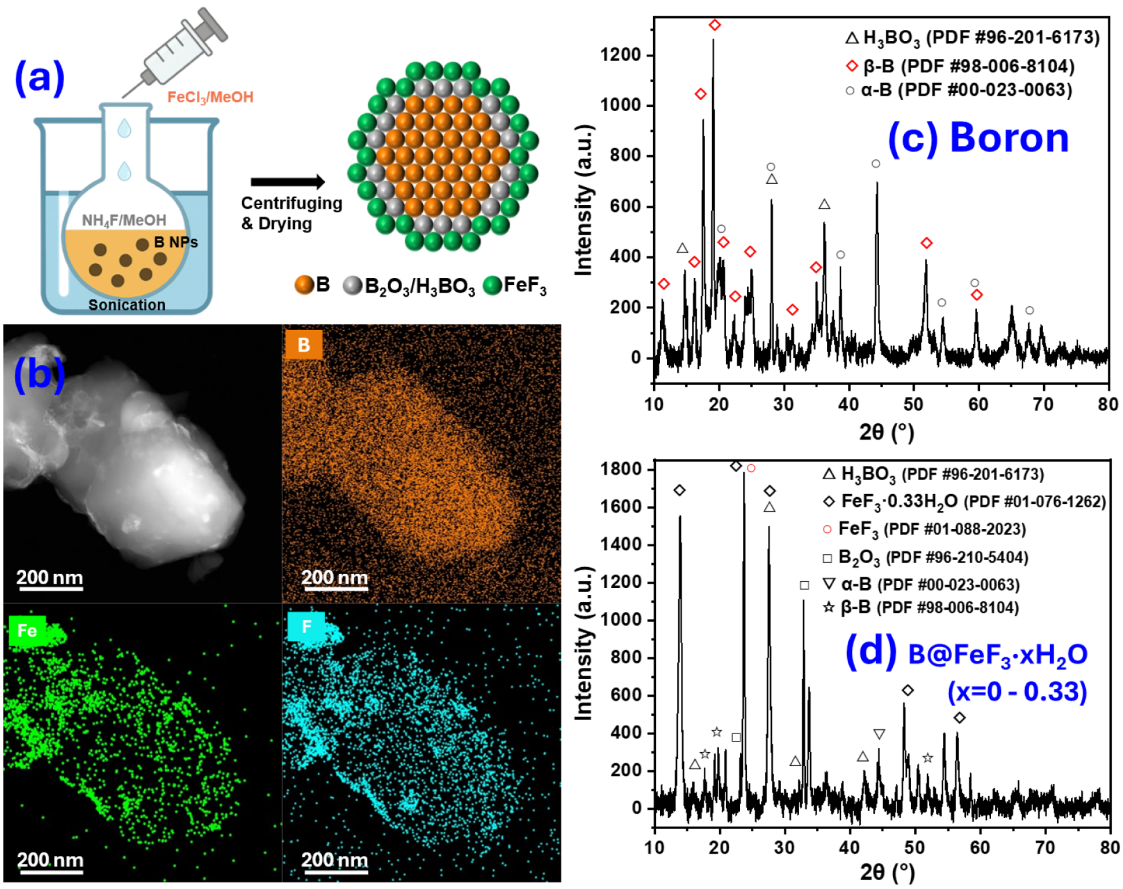

Figure 1. Synthesis and characterization: (a) illustration of the synthesis route of B@$FeF_3 \cdot xH_2O$ particles. (b) TEM-EDS micrographs showing the inhomogeneous coating of $FeF_3 \cdot xH_2O$. (c,d) Comparison of XRD characterization of nascent boron and B@$FeF_3 \cdot xH_2O$.

support on the oxide etching mechanism (including the proposed BF_3 gas generation pathway),[14,17,23] leaving gaps between fundamental mechanistic understanding of the surface interference chemistry and practical applications.[13,17,24] Transient gas-phase species could in principle be probed using high-sensitivity spectroscopic[25−27] or mass-spectrometric diagnostics,[28] yet direct application of these methods to validate oxide-etching pathways in boron systems remains scarce.[5]

Nanothermites are heterogeneous intermixed composites composed of nanometer-scale fuel and oxidizer particles.[29] Incorporating such nanoparticles into polymer matrices strongly increases slurry viscosity, which in turn makes conventional casting routes impractical and has limited practical implementation because achievable particle loading (and energy density) is low.[29] Direct-writing of solvent-based inks (extrusion 3D printing) offers a pragmatic balance of convenient and precise control for producing structural energetic materials: shear-thinning inks permit very high particle loading (~90 wt %) while maintaining printability, a small polymer binder fraction provides mechanical integrity without excessive nonenergetic mass, and processing with solvent improves handling safety.[29] Critically, direct-writing produces free-standing, geometrically defined parts that preserve nanoscale fuel−oxidizer contacts and enable direct, application-relevant combustion measurements (burn rate, flame temperature, regression behavior).[30] Furthermore, advanced high-speed diagnostics, including digital inline holography (DIH) and color pyrometry, enable real-time visualization of particle ejection, rupture, and combustion dynamics in the 3D-printed samples with high temporal and spatial resolution, providing direct insights into reaction-front evolution.

In this work, we synthesized B@$FeF_3 \cdot xH_2O$ binary composites using a one-pot solvent-based coating method and made the boron thermites into free-standing structures via direct-write 3D printing. We characterized the morphological structure of the synthesized B@$FeF_3 \cdot xH_2O$ particles with TEM-EDS and XRD. Combustion and ignition properties of their mixed composites with different oxidizers (O_2, Bi_2O_3, $KClO_4$) were investigated systematically using TGA-DSC and high-speed cameras. Holographic imaging and three-color pyrometry operated at high frame rates were employed to capture in-flight particle-scale combustion dynamics and corresponding temperature profiles. In particular, violent in-flight droplet explosions of the B@$FeF_3 \cdot xH_2O$/Bi_2O_3 nanothermites were observed, which are later linked to rapid gas releases. Additionally, T-jump time-of-flight mass spectrometry was utilized to identify gas-phase species (BF_3 and HF) and elucidate reaction mechanisms on the oxide removal. The proposed reaction of B_2O_3 with FeF_3 was then further confirmed in TGA experiments. These results provide both clear mechanistic insights into the role of fluoridated coatings and practical strategies in improving the combustion performance of energetic nanomaterials.

2. METHODS

2.1. Material Synthesis and Characteristics

Boron was coated with FeF_3 via a one-pot synthesis: the boron nanoparticles (~100 nm, 87 wt % active, US Research Nanomaterials) were first suspended with ultrasonication in methanol solutions containing NH_4F (Sigma-Aldrich, 98%). Subsequently, a methanol solution of $FeCl_3$ (Acros Organics, 98%) was slowly added with a syringe pump to form FeF_3 precipitate and deposit onto the surface of boron particles during sonication (see Figure 1(a) for a schematic illustration). The overall chemical reaction is in eq 1, where all other species are methanol-soluble except FeF_3.[15,31] The detailed synthesis formulation is listed in Table S1 in Supporting Information. Upon completion of the reaction, the synthesized particles were separated from the solution with centrifugation at 10000 rpm for 10 min and washed with methanol to remove byproducts (NH_4Cl), and finally dried in a vacuum oven.

$$FeCl_3 + 3NH_4F \rightarrow FeF_3(s) + 3NH_4Cl \qquad (1)$$

The coated boron particles were characterized by scanning transmission electron microscope (FEI Titan Themis 300) and X-ray diffraction (PANalytical Empyrean Series 2). As confirmed by TEM images and EDS mapping (Figure 1(b)), the resulting $B@FeF_3$ nanoparticles exhibit inhomogeneous FeF_3 coatings, and some FeF_3 bulk exists. EDS line scans of Fe and F show the coating thickness is ~5−10 nm, as shown in Figure S1. XRD in Figure 1(c−d) shows the comparison of the uncoated boron and the synthesized sample. Without coating, the boron sample is mainly composed of its β-phase (and partially in α-phase), while boric acid (H_3BO_3) also exists. Boron oxide in the nascent boron sample is probably amorphous and thus not observed in XRD. After coating, strong signals from FeF_3 and its hydrate $FeF_3{\cdot}0.33H_2O$ are observed, indicating the coating is composed of $FeF_3{\cdot}xH_2O$ (x = 0−0.33). Therefore, in the following context, the coated boron particles are abbreviated as $B@FeF_3{\cdot}xH_2O$. The relative mass fraction of the $FeF_3{\cdot}xH_2O$ coating was later varied in the range of 10−35 wt % to explore the effect of coating content (as detailed in Section 3.1).

2.2. TGA-DSC

Thermogravimetric analysis (TGA) and differential scanning calorimetry (DSC) of the nascent nanoboron (washed with MeOH), B_2O_3/FeF_3 mixture (Sigma-Aldrich), or synthesized $B@FeF_3{\cdot}xH_2O$ particles are performed in a NETZSCH STA 449 F3 Jupiter thermogravimetric analyzer. All samples (~1 mg each run) are heated to 1000 °C with a ramp rate of 10 $°C{\cdot}min^{-1}$ in oxygen or argon flow (50 $mL{\cdot}min^{-1}$) to characterize the mass changes and corresponding exothermic or endothermic reactions.

2.3. T-Jump/TOFMS and Ignition Characterization

T-Jump time-of-flight mass spectrometry (TOFMS) was performed to investigate the reaction mechanisms in the fabricated composites at high heating rates (~4×10^5 $°C{\cdot}s^{-1}$), as detailed previously.[11,28] A small quantity (5 mg) of the prepared nanoparticle composites was dispersed in hexane and sonicated for 10 min. The suspension was then drop-cast on a platinum wire (1 cm long, 76-μm diameter) soldered to copper leads of the electrical feedthroughs. The samples were then heated with a ~3 ms pulse under a high vacuum (10^{-6} Torr) to a maximum temperature of ~1000 °C. Following thermal activation by the pulse, the gas-phase species evolved during the reaction were ionized with a 70 eV electron gun and probed with a multichannel plate detector for 10 ms with a temporal resolution of 100 μs. These T-jump TOFMS measurements enable identification and time-resolved detection of transient species[32,33] formed during rapid oxide-etching reactions (such as BF_3 and HF).

The ignition characterization of the samples was carried out in an argon environment at 1 atm pressure. The ignition point was identified with a high-speed camera (Vision Research Phantom, version 12.0) operated at 67000 frames per second (fps), by correlating the optical emission obtained from the camera with the time and temperature obtained from wire heating, as shown in Figure S2.

2.4. Thermite Preparation with 3D Printing

The following manufacturing approach allows energetic composites to be fabricated as free-standing, densely packed, and geometrically defined structures rather than loose powder beds. High-loading boron nanothermite composites were prepared via 3D printing technique similar to our prior work.[29,30] Printable inks were prepared by dissolving a mixture of 4 wt % polyvinylidene fluoride (PVDF, from Sigma-Aldrich) and 6 wt % hydroxypropyl methylcellulose (HPMC, from Dow Chemical) in *N*,*N*-dimethylformamide (DMF, from Fisher Scientific) solvent. Then the metal fuel (synthesized $B@FeF_3$ or nascent boron nanoparticles) and the oxidizer, $KClO_4$ (Sigma-Aldrich) or Bi_2O_3 (80 nm, US Research Nanomaterials) at equivalence ratio (φ = 1, 90 wt % total loading), were added, vortexed, and ultrasonicated for 20 minutes, followed by 10 min mixing at 400 rpm in Thinky Mixer AR100 until homogeneous. The inks were directly written through 18-gauge nozzles onto heated glass substrates (70 °C to vaporize DMF), and the printed samples were cut into ~2 cm free-standing sticks. 3D printing (direct-writing) provides a controllable and safe approach to fabricate free-standing energetic architectures with high particle loading and mechanical integrity, overcoming the poor processability of loose thermite powders and enabling quantitative combustion measurements under realistic configurations.[29]

2.5. Regression Rate Measurement

The regression rate of 3D-printed thermite is calculated from the slope of a linear fitting curve from the flame front position of the thermite versus burning time, as measured using a high-speed camera (Vision Research Phantom Miro M110 paired with a Nikon AF Micro Nikkor lens) operating at 1000 fps. Prior to the experiments, the thermite was free-standing horizontally with one end held by tape, with a coiled NiCr ignition wire placed at the other end. Subsequently, the ignition coil is heated with direct current, simultaneously triggering the camera to capture the combustion process in real time. Representative snapshots of the regression rate test and linear fit are shown in Figure S3.

2.6. High-Speed Optical Diagnostics

The ejection of burning particles from the reaction zone of 3D-printed thermites was visualized using high-speed digital inline holography (DIH). A collimated continuous-wave 532 nm laser (Coherent Verdi V-6) was used for illumination. The beam was spatially filtered through a 5-μm pinhole and expanded to a 25 mm diameter using a pair of planoconvex lenses with focal lengths of 10 mm and 100 mm (Thorlabs, models P5W, C060TMD-A, and LA1509-A, respectively). The resulting in-line holograms were recorded using a high-speed CMOS camera (Phantom VEO 1310S, binning mode) operating at 100,000 fps with an exposure time of 9 μs. Infinity K2 Distamax long-distance microscope lenses (NTX tube with CF-4 objective) were used to achieve a spatial resolution of 2.8 $\mu m{\cdot}pixel^{-1}$ across a 0.90 × 0.67 mm field of view. To suppress broadband light emissions from the combustion zone, a narrow-band-pass optical filter (Thorlabs FLH532-4, 532 ± 2 nm) was installed in front of the detector. The optical focal plane was aligned between the fuel sample and the camera sensor to optimize the capture of diffraction patterns. The underlying principle of DIH is described in prior literature.[34−37] This configuration enabled high-contrast diffraction patterns generated by particles larger than ~3 μm to be captured and subsequently processed for three-dimensional tracking and sizing. The numerical reconstruction of particle fields was conducted using the Fresnel approximation.

Combustion dynamics at the microscopic scale were also recorded using high-speed color imaging, following methods described previously.[38,39] Microscopic imaging was conducted with a Phantom VEO 710L camera coupled to a long working distance microscope lens (Infinity Photo-Optical K2 DistaMax with CF-4 objective), achieving a spatial resolution of ~2.1 $\mu m{\cdot}pixel^{-1}$ from a working distance of ~54 mm. Two-color pyrometry was applied to the color

https://doi.org/10.1021/acsami.5c18742
ACS Appl. Mater. Interfaces XXXX, XXX, XXX−XXX

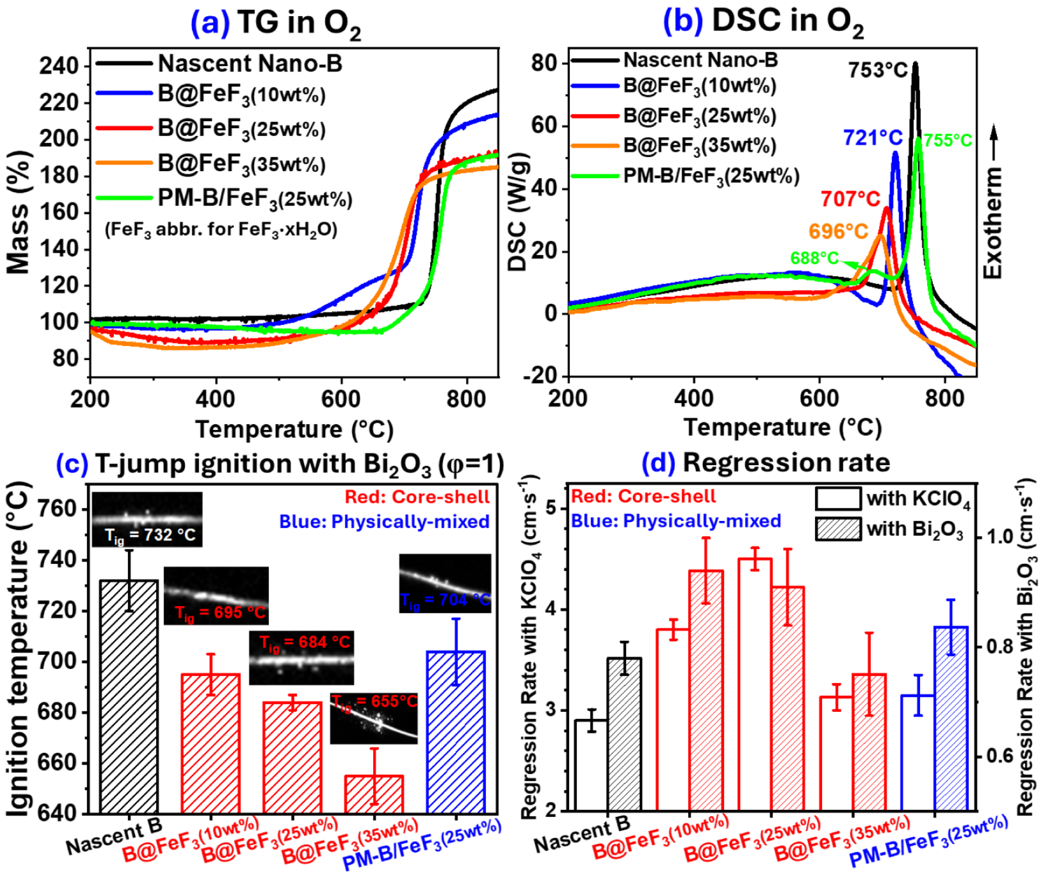

Figure 2. (a,b) TGA-DSC of B@$FeF_3·xH_2O$ (10−35 wt % coating, abbreviated as B@FeF_3) compared to nascent boron and physically mixed B/FeF_3 (25 wt %, labeled as PM-B/FeF_3) in O_2 environment at heating rate of 10 K·min^{-1}. (c) T-jump ignition temperature of B@$FeF_3·xH_2O$ with different coating contents and control samples. (d) Regression rate of burning B@$FeF_3·xH_2O$ thermite composites at varied coating contents and control samples with two different oxidizers (blank bars: $KClO_4$; hatched bars: Bi_2O_3).

imaging data to estimate surface temperatures across the field of view, following established techniques.[38,40] Raw red and blue intensity values were extracted by debayering the Bayer-patterned sensor output. Pixel-wise temperature estimation was performed by calculating intensity ratios between the B/R color channels and comparing them to theoretical blackbody curves under the assumption of graybody emission. Calibration was conducted using blackbody sources (ThorLabs SLS201L and Micron M390), resulting in a temperature estimation uncertainty of ∼200−300 K.

3. RESULTS AND DISCUSSION

3.1. Thermal Analysis and Combustion Performance

The TGA-DSC results of the nascent B and B@$FeF_3·xH_2O$ (coating 10−35 wt %) powders in an O_2 atmosphere are shown in Figure 2(a,b). For nascent boron, a mass gain occurs at ∼730−820 °C from oxidation to B_2O_3. In contrast, the B@$FeF_3·xH_2O$ samples exhibit slight mass losses of <10% between 200−350 °C, likely resulting from dehydration and decomposition of the $FeF_3·xH_2O$ coating layer;[41] followed by the mass gain from ∼650 −750 °C, indicating that both the start and completion of the oxidation process are earlier for the coated boron particles. The DSC curves in Figure 2(b) show that oxidation of nascent boron has a sharp exotherm centered at 753 °C; while for B@$FeF_3·xH_2O$ samples, broader exotherms appear at lower temperatures of 696−721 °C and shift toward lower temperatures as coatings get thicker, also indicating an earlier onset of oxidation. Interestingly, the physically mixed bicomposite B/FeF_3 (25 wt %, labeled as PM) exhibits two exotherms at 688 and 755 °C, where the earlier small peak likely corresponds to B + O_2 oxidation after partial oxide-layer removal at limited interface contacts between B and FeF_3, whereas the majority of boron still undergoes oxidation at the higher temperature similar to nascent boron. This control experiment confirms that the core−shell geometry provides improved interfacial contact and surface reactions. The TGA-DSC also shows that the coating is not without drawbacks, lowering boron active content: (1) The total mass gain in the coated boron is lower than that of nascent boron because of the 10−35 wt % FeF_3 coatings; (2) The area integration of the DSC exothermic peaks also indicates an ∼25% reduction of heat release in the 25 wt % coated boron sample (Figure S4).

Such a reduction in oxidation temperature observed in TGA is consistent with results from the following T-jump ignition experiments (as detailed in Section 2.3 and Figure S2). After physically mixed with the Bi_2O_3 oxidizer by sonication in hexane, the boron nanoparticles (or B@$FeF_3·xH_2O/Bi_2O_3$) were drop-cast onto Pt wires for T-jump ignition tests at high heating rates within 3 ms (∼4 × 10^5 K·s^{-1}). As shown in Figure 2(c), the B@$FeF_3·xH_2O/Bi_2O_3$ reaction initiates at a lower temperature compared to uncoated B/Bi_2O_3 (732 °C). The ignition temperatures fall in the range of ∼655−695 °C for 10−35 wt % B@$FeF_3·xH_2O$, with the 35 wt % coating exhibiting the lowest onset. The control experiment of physically mixed B/FeF_3 (25 wt %) ignites at 704 °C, which is an improvement over nascent boron but higher than the coated boron at the same FeF_3 loading, underscoring that the core−shell geometry helps ignition.

To compare their regression rates in combustion applications, free-standing thermite samples of B or $B@FeF_3{\cdot}xH_2O$ were 3D-printed after being physically mixed with different oxidizers ($KClO_4$ or Bi_2O_3) using PVDF/HPMC as binder (as detailed in Section 2.4). We adopt a direct-writing approach for the following reasons: Direct-writing 3D printing provides precise control of composition and architecture, enabling high particle loadings (90 wt % for nanothermites in this work) while maintaining mechanical integrity comparable to polymeric solids. In our study, the nano-$B/FeF_3{\cdot}xH_2O$ inks are shear-thinning and printable, forming uniform micro-architectures that improve particle contact and heat transfer during combustion. This approach also reduces handling sensitivity by dispersing the energetic nanoparticles in a binder matrix and ink solvent during processing, greatly enhancing safety compared with dry mixing. More importantly, printed thermite architecture allows direct measurement of regression rates and energy release under application-relevant geometries. Thus, 3D printing offers a pathway to mechanically robust, tunable, and safer energetic structures, a key step toward the practical implementation of nanoscale boron thermites.

The combustion process was measured with a high-speed camera, as detailed in Section 2.5 and Figure S3. The resultant regression rates are compared in Figure 2(d). For the $B/KClO_4$ thermites, the composite with $FeF_3{\cdot}xH_2O$ coating exhibits faster combustion, and the regression rate increases with coating thickness (until 25 wt % coating): Compared to bare B, the regression rate of the 10 and 25 wt % coating increases by 30% and 55% respectively. While for B/Bi_2O_3 thermites, both 10 and 25 wt % coating show similar regression rate enhancement of ∼20%. Thicker coating of $FeF_3{\cdot}xH_2O$ of 35 wt % was also tested, resulting in slower regression rates, likely due to the reduced active content or less effective fuel-oxidizer interfacial contact. These results suggest that the optimal $FeF_3{\cdot}xH_2O$ coating balancing interfacial oxidation enhancement with minimal loss of active content lies ∼25 wt %. The physically mixed B/FeF_3 (25 wt %) sample shows higher regression rates than bare B but remains lower than the 25 wt % core−shell sample, further indicating that the coating geometry helps the interfacial reactions.

3.2. High-Speed Optical Diagnostics of Combustion of 3D-Printed Nanothermites

High-speed DIH was employed to investigate the microscopic view of particle evolution near the flame front. Experimental details are in Section 2.6 and Figure S5(a). As shown in Figure 3(a−b), the B/Bi_2O_3 thermite sticks generate numerous molten spherical droplets that emanate from the flame front, likely due to the aggregation of molten Bi_2O_3 (melting point 817 °C). Particle size distributions are similar in both thermites, with an average of 43 μm, as shown in Figure S5(b−c) . In comparison, Figure 3(d−e) presents the color imaging (left) and temperature mapping (right) using 2-color pyrometry of the particles, showing that the average temperature of both coated and uncoated samples is ∼2000 K, which is likely capped by the boiling point of Bi_2O_3 and B_2O_3 (1890 and 1860 °C, respectively).

Interestingly, highly reactive particle rupture dynamics were observed only with the coated boron samples. Figure 3(c) shows the explosion process of a flying droplet ejected from the flame front of the $B@FeF_3{\cdot}xH_2O/Bi_2O_3$ thermite with a time interval of 10 μs. The snapshot at 10 μs shows the initial spherical particle shape and its size (∼100 μm). At 20−30 μs, the particle quickly expanded to more than 2× of the initial outer diameter, likely due to the quick generation of gases from inside the particle (explored in more detail in Section 3.3). At ∼40−90 μs, the expanded particle explodes, generating smaller secondary particles that fly in different directions.

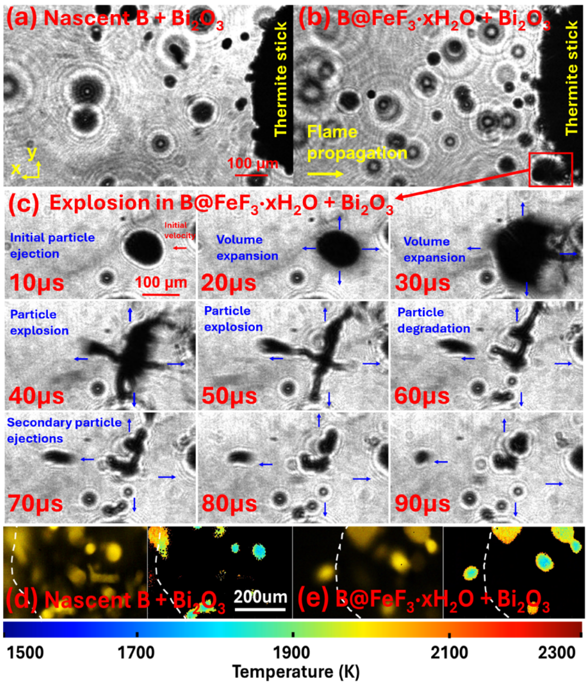

Figure 3. DIH snapshots during combustion of (a) B/Bi_2O_3 or (b) $B@FeF_3{\cdot}xH_2O$(25 wt %)/Bi_2O_3 thermite (c) time-resolved explosion process of a flying particle ejected from the thermite flame front of $B@FeF_3{\cdot}xH_2O/Bi_2O_3$ and (d,e) corresponding two-color pyrometry.

3.3. Reaction Mechanism via Rapid Heating Time-of-Flight Mass Spectrometry

To investigate the role of the $FeF_3{\cdot}xH_2O$ coating in boron combustion, gaseous species evolved during the pyrolysis of $B@FeF_3{\cdot}xH_2O$ and its reaction with Bi_2O_3 were analyzed using T-jump/TOFMS at a high heating rate (∼4×10^5 $K{\cdot}s^{-1}$). As shown in Figure 4(a), compared to the nascent B particles (red curve), $B@FeF_3{\cdot}xH_2O$ (orange) generates signals of HF and BF_2 (m/z = 20 and 49) while reducing the signals associated with the native B_2O_3/H_3BO_3 surface layer (m/z = 43, 57, and 70 of BO_2, $H_3B_2O_2$, and B_2O_3). The TOFMS temporal profiles of HF and BF_2 in Figure 4(b) show that HF generation begins around 350 °C from thermal decomposition of $FeF_3{\cdot}0.33H_2O$; Above ∼630 °C, as shown in eq 2, FeF_3 reacts with B_2O_3 to form BF_3, which subsequently fragments into BF_2 under electron-impact ionization (see Figure S7 and pink curve in Figure 4a).[42] The reaction Gibbs free energy and its change with temperature are shown in Figure 4(c), indicating that this entropy-driven reaction becomes spontaneous when the temperature gets above 478 °C. Further confirmation was obtained from TG measurement of the physically mixed B_2O_3 and FeF_3 (1:2 mol) in an Ar environment, represented by the black curve in Figure 4(c), which shows a total mass loss of 42% after heating to >800 °C. The postheated products of B_2O_3 and FeF_3 were then characterized with XRD, showing hexagonal hematite (Fe_2O_3) as the primary solid-phase product (Figure 4d). In contrast, the heated B_2O_3 (red curve

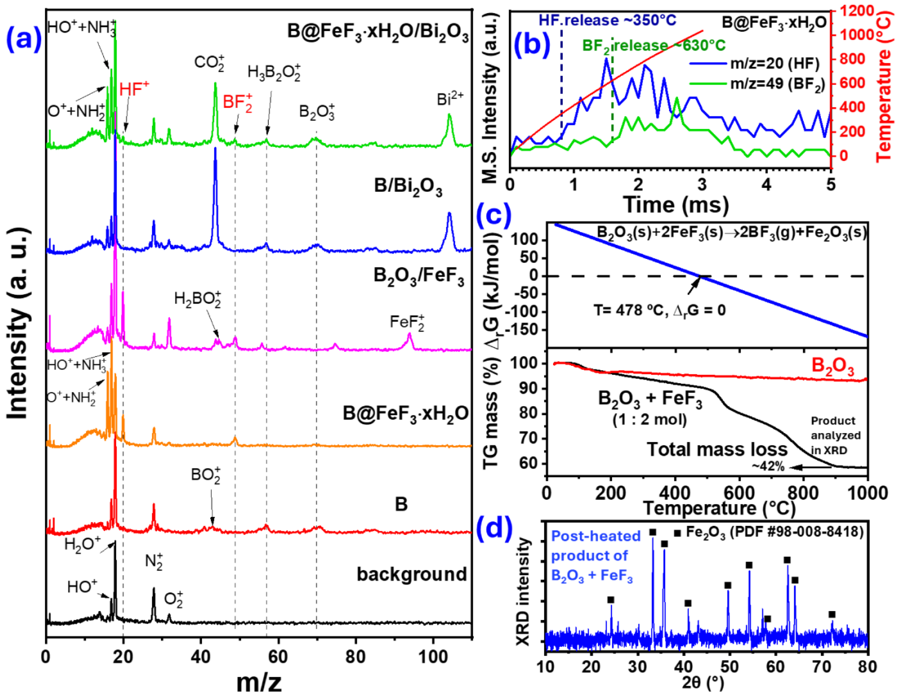

Figure 4. (a) T-jump/TOFMS spectrometry for background, B, B@FeF$_3$·xH$_2$O, physically mixed B$_2$O$_3$/FeF$_3$, B/Bi$_2$O$_3$ and B@FeF$_3$·xH$_2$O(25 wt %)/Bi$_2$O$_3$ composites; (b) temporal evolution of HF and BF$_2$ from B@FeF$_3$·xH$_2$O measured with T-jump/TOFMS; (c) Gibbs free energy of B$_2$O$_3$ + FeF$_3$ reaction, and TG of pure B$_2$O$_3$ versus the mixture of B$_2$O$_3$ and FeF$_3$ (1:2 mol) in Ar; and (d) XRD of postheated product of B$_2$O$_3$ + FeF$_3$ (1:2 mol) in Ar.

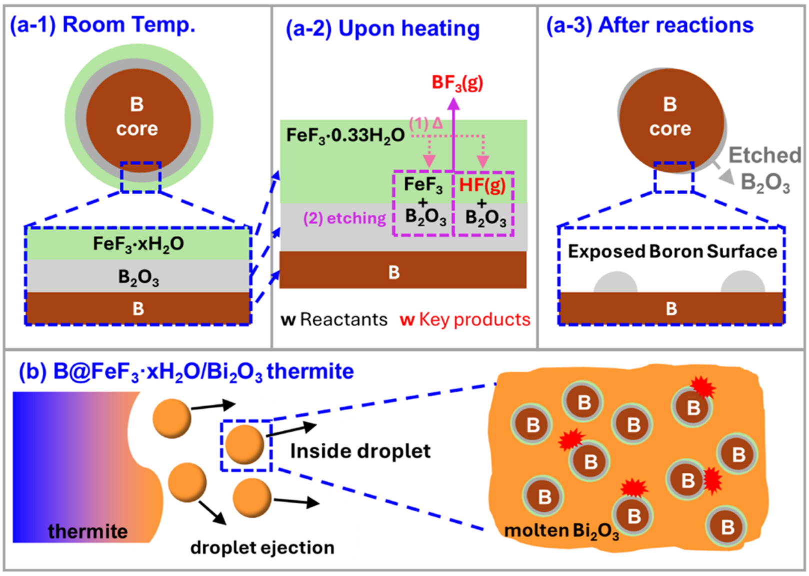

Figure 5. (a) Mechanism illustration of interfacial gas-generation reactions of B@FeF$_3$·xH$_2$O nanoparticles; (b) explosion mechanism of the in-flight droplets ejected from the B@FeF$_3$·xH$_2$O/Bi$_2$O$_3$ thermite composite.

in Figure 4c) only shows slight mass loss of ~6% at 100−200 °C, mainly due to the loss of water from boric acid impurities. FeF$_3$ is also thermally stable below 800 °C, as shown by TG in Figure S6, consistent with previous studies.[43] This comparison further supports the formation mechanism of gas-phase species BF$_3$ from

$$B_2O_3 + 2FeF_3 \rightarrow 2BF_3(g) + Fe_2O_3$$
$$(\Delta G_r = -50\ \mathrm{kJ{\cdot}mol^{-1}}\ \mathrm{at}\ T = 630°\mathrm{C}) \quad (2)$$

For the B/Bi$_2$O$_3$ mixture (blue curve in Figure 4a), Bi$_2$O$_3$ generates O$_2$ and Bi fragments (m/z = 32 and 104 for Bi^{2+}); while for the coated mixture (green curve of B@FeF$_3$·xH$_2$O/Bi$_2$O$_3$), the mass spectrum shows additional HF and BF$_2$ signals. Notably, the HF/BF$_2$ intensity ratio in B@FeF$_3$·xH$_2$O decreases from 1.5 to 0.5 with the addition of Bi$_2$O$_3$, and the HF/(O + NH$_2$) ratio decreases from 0.5 to 0.3. This trend reflects more conversion of HF into BF$_3$, possibly facilitated by molten Bi$_2$O$_3$ droplets around the nanoparticles acting as a cap that delays the HF gas escaping and promotes the HF + B$_2$O$_3$ reaction, as shown in eqs 3−4. Other possible reaction pathways were also investigated but excluded as major contributors with additional TOFMS experiments, as detailed in Figure S8.

$$FeF_3 \cdot 0.33H_2O \rightarrow (1 - 2x)FeF_3 + xFe_2O_3 + 6xHF(g) + (0.33 - 3x)H_2O(g) \quad (3)$$

$$6HF(g) + B_2O_3 \rightarrow 2BF_3(g) + 3H_2O(g) \quad (4)$$

The overall mechanism of the enhanced combustion is illustrated in Figure 5, showing that the $FeF_3 \cdot xH_2O$ coating enhances combustion by facilitating the removal of the passivating B_2O_3 layer on boron nanoparticles. Upon heating, FeF_3 reacts with B_2O_3 to produce volatile BF_3, thereby exposing the underlying reactive boron surface to surrounding oxidizers. In addition, $FeF_3 \cdot 0.33H_2O$ also decomposes to release HF, which would be trapped by molten Bi_2O_3 and then reacts with B_2O_3 to produce more BF_3.

This gas generation likely accounts for the in-flight explosion observed in the DIH video of the composite of $B@FeF_3 \cdot xH_2O/Bi_2O_3$. Assuming that the composition within the molten Bi_2O_3 droplet remains as prepared, which is 4.4 wt % B, 0.8 wt % B_2O_3 (based on 87% active content for B nanoparticles), 1.7 wt % $FeF_3 \cdot xH_2O$, and 93.1 wt % Bi_2O_3, when all FeF_3 participates in forming BF_3 gas, the volumetric expansion is calculated to be significant: At ∼1090 K (Bi_2O_3 melting point) and 1 atm, the estimated volume ratio of generated BF_3 gas to the liquid composite droplet is $\frac{V_{\mathrm{BF_3\ gas}}}{V_{\mathrm{droplet}}} \sim 100$. This estimation supports the hypothesis that rapid BF_3 generation can cause droplet rupture and explosion during combustion.

Table S2 compares thermochemical properties[42,44−46] of the different fluorinated coating materials (LiF, FeF_3, CoF_2, CuF_2, BiF_3) that have been explored as coating materials in previous studies.[5] Notably, all of their etching reactions with B_2O_3 are endothermic and nonspontaneous at room temperature, but the positive entropy change associated with the formation of gaseous BF_3 or BOF drives these reactions to become spontaneous at elevated temperatures. The temperatures at which the etching reactions become spontaneous (T_{sp}) and the mass of each metal fluoride required to consume one mole of B_2O_3 oxide are also summarized in Table S2. Although LiF removes the largest amount of B_2O_3 per unit mass, its spontaneous reaction temperature is very high ($T_{sp} \sim 1200$ °C). In contrast, FeF_3 exhibits a relatively low T_{sp} (478 °C) and also removes more B_2O_3 per unit mass than CoF_2, CuF_2, and BiF_3. Compared with previous work by Qin et al.[17] (see Table S3) who prepared micron-sized B/FeF_3 composites by high-speed ball milling, our work (1) targets nanoparticles (∼100 nm) and therefore a different size-dependent reactivity regime, (2) uses a one-pot solvent-based precipitation to form core−shell $FeF_3 \cdot xH_2O$ coatings that is difficult to achieve by ball milling for nanoparticles, and (3) provides direct T-jump/TOFMS detection of HF and BF_2 (BF_3 proxy) under rapid heating, giving molecular evidence for oxide removal that was only inferred previously. Furthermore, whereas previous works used loosely packed powders for combustion tests, we (4) fabricate free-standing 3D-printed nanothermite components and quantify regression-rate improvements (up to +55%) under application-relevant tests, and (5) use DIH to visualize gas-driven droplet rupture and particle-scale fragmentation.[47]

4. CONCLUSION

This work demonstrates a one-pot coating method as a strategy to overcome the long-standing ignition barrier of boron fuels. Coating boron nanoparticles with $FeF_3 \cdot xH_2O$ lowers their ignition temperature and accelerates combustion (burn rates increased by up to 55%) by chemically etching away the refractory B_2O_3 shell. High-speed optical diagnostics and T-jump mass spectrometry revealed that the $FeF_3 \cdot xH_2O$ coating reacts with the oxide shell and releases gas-phase BF_3 and HF, which drive microexplosive fragmentation and rapid energy release of the boron fuel. Overall, this work shows how fluorinated coating serves as an effective additive by removing passivating oxides while introducing gas-phase reactions, offering both mechanistic insights and practical strategies to realize boron's high-energy potential in propellant or explosive applications.

■ ASSOCIATED CONTENT

Supporting Information

The Supporting Information is available free of charge at https://pubs.acs.org/doi/10.1021/acsami.5c18742.

> Formulation of coating method; thermodynamic comparisons of the different fluorinated coating materials; comparison with previous studies on B/FeF_3; line scan of STEM-EDS; T-jump ignition setup and snapshots; regression rate measurements; active contents from TGA and the integration of DSC; DIH setup and histograms of particle sizes; TGA of FeF_3; mass spectrometry reference of BF3; T-jump/TOFMS spectra of more control experiments (PDF)

■ AUTHOR INFORMATION

Corresponding Author

Michael R. Zachariah − *University of California, Riverside, California 92521, United States;* orcid.org/0000-0002-4115-3324; Email: mrz@engr.ucr.edu

Authors

Lei Yang − *University of California, Riverside, California 92521, United States;* orcid.org/0000-0002-1094-8642
Yuan Qin − *University of California, Riverside, California 92521, United States*
Gabriel Lopez − *University of California, Riverside, California 92521, United States*
Erik Hagen − *University of California, Riverside, California 92521, United States*

Complete contact information is available at: https://pubs.acs.org/10.1021/acsami.5c18742

Author Contributions

[#]L.Y. and Y.Q. contributed equally to this work. L.Y. and Y.Q.: Formal analysis, data curation, writing—original draft. G.L. and E.H.: Data curation. M.R.Z.: Supervision,resources, project administration, methodology, investigation, funding acquisition, conceptualization, writing—review and editing.

Notes

The authors declare no competing financial interest.

■ ACKNOWLEDGMENTS

This work was supported by the DTRA-MSEE URA and the AFOSR.

■ REFERENCES

(1) Dreizin, E. L. Metal-Based Reactive Nanomaterials. *Prog. Energy Combust. Sci.* **2009**, *35* (2), 141−167.

(2) Sullivan, K.; Young, G.; Zachariah, M. R. Enhanced Reactivity of Nano-B/Al/CuO MIC's. *Combust. Flame* **2009**, *156* (2), 302−309.

(3) Young, G.; Sullivan, K.; Zachariah, M. R.; Yu, K. Combustion Characteristics of Boron Nanoparticles. *Combust. Flame* **2009**, *156* (2), 322−333.

(4) Sundaram, D.; Yang, V.; Yetter, R. A. Metal-Based Nanoenergetic Materials: Synthesis, Properties, and Applications. *Prog. Energy Combust. Sci.* **2017**, *61*, 293−365.

(5) Zhang, C.; Kou, Y.; Xiao, L.; Hu, Y.; Lu, Q.; Zhao, F.; Hu, Y.; Jiang, W.; Yang, Y.; Hao, G. Research Progress on the Modification of B and Al High-Energy Fuels for Powder Fuel Ramjet Applications. *ACS Appl. Mater. Interfaces* **2025**, *17* (8), 11522−11551.

(6) Perez, J. P. L.; Yu, J.; Sheppard, A. J.; Chambreau, S. D.; Vaghjiani, G. L.; Anderson, S. L. Binding of Alkenes and Ionic Liquids to B−H-Functionalized Boron Nanoparticles: Creation of Particles with Controlled Dispersibility and Minimal Surface Oxidation. *ACS Appl. Mater. Interfaces* **2015**, *7* (18), 9991−10003.

(7) Yeh, C. L.; Kuo, K. K. Ignition and Combustion of Boron Particles. *Prog. Energy Combust. Sci.* **1996**, *22* (6), 511−541.

(8) Wang, Y.; Xu, F.; Issac Paul, G.; Vidales Pasos, E.; Shi, K.; Wagner, B.; Mangolini, L.; Zachariah, M. R. Role of Surface Tension on Heat Feedback and Power from Energetic Composites. *ACS Appl. Mater. Interfaces* **2024**, *16*, 42100−42108.

(9) Jiang, Y.; Dincer Yilmaz, N. E.; Barker, K. P.; Baek, J.; Xia, Y.; Zheng, X. Enhancing Mechanical and Combustion Performance of Boron/Polymer Composites via Boron Particle Functionalization. *ACS Appl. Mater. Interfaces* **2021**, *13* (24), 28908−28915.

(10) Baek, J.; Jiang, Y.; Demko, A. R.; Jimenez-Thomas, A. R.; Vallez, L.; Ka, D.; Xia, Y.; Zheng, X. Effect of Fluoroalkylsilane Surface Functionalization on Boron Combustion. *ACS Appl. Mater. Interfaces* **2022**, *14* (17), 20190−20196.

(11) Yang, L.; Zhou, Y.; Chowdhury, M.; Qin, Y.; Dickson, M. M.; Zachariah, M. R. Synergistic Transition Multi-Metal Coatings Drive Sub-Melting-Point Reaction of Aluminum. *Chem. Eng. J.* **2025**, *519*, 164794.

(12) Zhou, Y.; Yang, L.; Vasudevan, A. K.; Dickson, M.; Chowdhury, M.; Shi, K.; Zachariah, M. R. Nickel-Coated Aluminum Nanoparticles for Modulating Ignition Temperature: Interfacial Chemistry and Mechanism. *ACS Appl. Eng. Mater.* **2025**, *3* (8), 2346−2353.

(13) Liu, R.; Yang, D.; Xiong, K.; Wang, Y.-L.; Yan, Q.-L. Fabrication and Characterization of Multi-Scale Coated Boron Powders with Improved Combustion Performance: A Brief Review. *Def. Technol.* **2024**, *31*, 27−40.

(14) Yan, L.; Zhu, B.; Chen, J.; Sun, Y. Study on Nano-Boron Particles Modified by PVDF to Enhance the Combustion Characteristics. *Combust. Flame* **2023**, *248*, 112556.

(15) Valluri, S. K.; Schoenitz, M.; Dreizin, E. Bismuth Fluoride-Coated Boron Powders as Enhanced Fuels. *Combust. Flame* **2020**, *221*, 1−10.

(16) Valluri, S. K.; Schoenitz, M.; Dreizin, E. Boron-Metal Fluoride Reactive Composites: Preparation and Reactions Leading to Their Ignition. *J. Propuls. Power* **2019**, *35* (4), 802−810.

(17) Qin, Y.; Zou, J.; Yu, H.; Huang, X.; Song, Y.; Li, F.; Liu, J. S. O. P. Ignition and Combustion Performance of High Activity Boron-Based Composite Micro-Units. *Combust. Flame* **2025**, *273*, 113931.

(18) Ka, D.; Baek, J.; Jiang, Y.; Huynh, A. H.; Gross, G. R.; Kong, D.; Xia, Y.; Zheng, X. Mechanical and Combustion Properties of Fluoroalkylsilane Surface-Functionalized Boron/HTPB Composite. *Combust. Flame* **2024**, *268*, 113621.

(19) Chen, Y.; Ou, J.; Yang, T.; Zhu, B.; Sun, Y. Synergetic Modification of Micron-Sized Boron Powder with Fluoroelastomer and Glycidyl Azide Polymer to Improve Its Ignition and Combustion. *Combust. Flame* **2025**, *273*, 113973.

(20) Zeng, X.; Yu, S.; Wang, J.; Wang, J.; Gan, Y.; Wei, X.; Chen, J.; Zhang, X. Synergy BiF_3 and Bi_2O_3 to Enhance the Ignition and Combustion Performance of Boron. *Combust. Flame* **2025**, *275*, 114037.

(21) Mnoyan, A.; Chroay, S.; Kim, M.; Kirakosyan, K.; Shin, W. G. Novel Sodium Tetrafluoroborate Additive for Enhancing Boron's Energetic Performance. *Fuel* **2026**, *405*, 136504.

(22) Agarwal, P. P. K.; Jensen, D.; Chen, C.-H.; Rioux, R. M.; Matsoukas, T. Surface-Functionalized Boron Nanoparticles with Reduced Oxide Content by Nonthermal Plasma Processing for Nanoenergetic Applications. *ACS Appl. Mater. Interfaces* **2021**, *13* (5), 6844−6853.

(23) Li, C.; Song, H.; Xu, C.; Li, C.; Jing, J.; Ye, B.; Wang, J.; An, C. Reactivity Regulation of B/KNO_3/PVDF Energetic Sticks Prepared by Direct Ink Writing. *Chem. Eng. J.* **2022**, *450*, 138376.

(24) Yetter, R. A.; Dryer, F. L.; Rabitz, H.; Brown, R. C.; Kolb, C. E. Effect of Fluorine on the Gasification Rate of Liquid Boron Oxide Droplets. *Combust. Flame* **1998**, *112* (3), 387−403.

(25) Yang, L.; Zhang, J. Effect of Carbon Chain Length on Nascent Yields of Stabilized Criegee Intermediates in Ozonolysis of a Series of Terminal Alkenes. *J. Am. Chem. Soc.* **2024**, *146* (35), 24591−24601.

(26) Campos-Pineda, M.; Yang, L.; Zhang, J. Direct Measurement of the Criegee Intermediate CH_2OO in Ozonolysis of Ethene. *Nat. Commun.* **2025**, *16* (1), 6515.

(27) Yang, L.; Campos-Pineda, M.; Zhang, J. Low-Pressure and Nascent Yields of Thermalized Criegee Intermediate in Ozonolysis of Ethene. *J. Phys. Chem. Lett.* **2022**, *13* (49), 11496−11502.

(28) Rehwoldt, M. C.; Wang, Y.; Xu, F.; Ghildiyal, P.; Zachariah, M. R. High-Temperature Interactions of Metal Oxides and a PVDF Binder. *ACS Appl. Mater. Interfaces* **2022**, *14* (7), 8938−8946.

(29) Wang, H.; Shen, J.; Kline, D. J.; Eckman, N.; Agrawal, N. R.; Wu, T.; Wang, P.; Zachariah, M. R. Direct Writing of a 90 Wt% Particle Loading Nanothermite. *Adv. Mater.* **2019**, *31* (23), 1806575.

(30) Wang, H.; Biswas, P.; Kline, D. J.; Zachariah, M. R. Flame Stand-off Effects on Propagation of 3D Printed 94 Wt% Nanosized Pyrolants Loading Composites. *Chem. Eng. J.* **2022**, *434*, 134487.

(31) Bai, Y.; Zhou, X.; Zhan, C.; Ma, L.; Yuan, Y.; Wu, C.; Chen, M.; Chen, G.; Ni, Q.; Wu, F.; Shahbazian-Yassar, R.; Wu, T.; Lu, J.; Amine, K. 3D Hierarchical Nano-Flake/Micro-Flower Iron Fluoride with Hydration Water Induced Tunnels for Secondary Lithium Battery Cathodes. *Nano Energy* **2017**, *32*, 10−18.

(32) Lucas, M.; Qin, Y.; Yang, L.; Sun, G.; Zhang, J. Ultraviolet Photochemistry of the 2-Buten-2-Yl Radical. *Phys. Chem. Chem. Phys.* **2024**, *26*, 26966−26975.

(33) Lucas, M.; Qin, Y.; Yang, L.; Sun, G.; Zhang, J. Ultraviolet Photodissociation Dynamics of the 1-Methylallyl Radical. *J. Phys. Chem. A* **2024**, *128*, 5556−5566.

(34) Chen, Y.; Guildenbecher, D. R.; Hoffmeister, K. N. G.; Cooper, M. A.; Stauffacher, H. L.; Oliver, M. S.; Washburn, E. B. Study of Aluminum Particle Combustion in Solid Propellant Plumes Using Digital In-Line Holography and Imaging Pyrometry. *Combust. Flame* **2017**, *182*, 225−237.

(35) Huang, J.; Li, S.; Cai, W.; Qian, Y.; Berrocal, E.; Aldén, M.; Li, Z. Quantification of the Size, 3D Location and Velocity of Burning Iron Particles in Premixed Methane Flames Using High-Speed Digital in-Line Holography. *Combust. Flame* **2021**, *230*, 111430.

(36) Mazumdar, Y. C.; Smyser, M. E.; Heyborne, J. D.; Slipchenko, M. N.; Guildenbecher, D. R. Megahertz-Rate Shock-Wave Distortion Cancellation via Phase Conjugate Digital in-Line Holography. *Nat. Commun.* **2020**, *11* (1), 1129.

(37) Vasudevan, A. K.; Hagen, E.; Zhou, Y.; Shi, K.; Yang, L.; Zachariah, M. R. In-Situ Growth of Nanoaluminum in Hydroxyl Terminated Polybutadiene and Combustion Characteristics. *Fuel* **2026**, *407*, 137273.

(38) Wang, Y.; Hagen, E.; Biswas, P.; Wang, H.; Zachariah, M. R. Imaging the Combustion Characteristics of Al, B, and Ti Composites. *Combust. Flame* **2023**, *252*, 112747.

(39) Wang, H.; Julien, B.; Kline, D. J.; Alibay, Z.; Rehwoldt, M. C.; Rossi, C.; Zachariah, M. R. Probing the Reaction Zone of Nanolaminates at ∼ μs Time and ∼ μm Spatial Resolution. *J. Phys. Chem. C* **2020**, *124* (25), 13679−13687.

(40) Jacob, R. J.; Kline, D. J.; Zachariah, M. R. High Speed 2-Dimensional Temperature Measurements of Nanothermite Composites: Probing Thermal vs. Gas Generation Effects. *J. Appl. Phys.* **2018**, *123* (11), 115902.

(41) Burbano, M.; Duttine, M.; Borkiewicz, O.; Wattiaux, A.; Demourgues, A.; Salanne, M.; Groult, H.; Dambournet, D. Anionic Ordering and Thermal Properties of $FeF_3 \cdot 3H_2O$. *Inorg. Chem.* **2015**, *54* (19), 9619−9625.

(42) NIST Mass Spectrometry Data Center, William E. Wallace, director, Mass Spectra. *NIST Chemistry WebBook, NIST Standard Reference Database Number 69*. Linstrom, P. J.; Mallard, W. G., Eds.; National Institute of Standards and Technology: Gaithersburg MD, 2011.

(43) Liu, P.; Li, X.; Cheng, L.; Zhu, X.; Li, Y.; Song, D. Preparation and Characterization of N-Al/FeF_3 Nanothermite. *Chem. Eng. J.* **2018**, *331*, 850−855.

(44) Hildenbrand, D. L.; Theard, L. P.; Saul, A. M. Transpiration and Mass Spectrometric Studies of Equilibria Involving BOF(g) and $(BOF)_3$(g). *J. Chem. Phys.* **1963**, *39* (8), 1973−1978.

(45) Farber, M.; Blauer, J. The Heat of Formation and Entropy of BOF. *Trans. Faraday Soc* **1962**, *58*, 2090−2094.

(46) Cubicciotti, D. Thermodynamic Properties of Bismuth Trifluoride. *J. Electrochem. Soc.* **1968**, *115* (11), 1138.

(47) Yang, L.; Shi, K.; Zhou, Y.; Chowdhury, M.; Anis, A.; Zachariah, M. R. Thermal and holography imaging of heat feedback enables strategies to drive sustained combustion in highly reactive thermite composites. *Chem. Eng. J.* **2026**, *527*, 171223.